ISSN 1385-8947

ELSEVIER

CEJ

CHEMICAL ENGINEERING JOURNAL

Actions for selected articles

Select all / Deselect all

Download PDFs

Export citations

Show all article previews

Contents

Research article ● Full text access

A blue light 3D printable hydrogel with water absorption, antibacterial, and hemostatic properties for skin wound healing

Xiu-Chong He, Xiu-Ning Chen, Yi-Hao Liu, Xinyu Zhong, ... Peng-Fei Zheng

Article 152439

View PDF Article preview

Research article ● Full text access

Potential-dependent photo-electro-catalysis coupling mechanism for methanol oxidation: A case study over Pt/Cu-Nb_2O_5 nanorod arrays

Shixu Song, Yan Zhao, Qisen Jia, Wanqing Yu, ... Luhua Jiang

Article 152550

View PDF Article preview

Research article ● Full text access

La promoted Ni^0-$Ni^{\delta+}$ synergistic interaction for rapid and deep hydrogenation of liquid organic hydrogen carriers

FEEDBACK

Chemical Engineering Journal 493 (2024) 152439

Contents lists available at ScienceDirect

Chemical Engineering Journal

journal homepage: www.elsevier.com/locate/cej

A blue light 3D printable hydrogel with water absorption, antibacterial, and hemostatic properties for skin wound healing

Xiu-Chong He [a,1], Xiu-Ning Chen [b,1], Yi-Hao Liu [c], Xinyu Zhong [d], Lei Qiang [b], Hong-Qin Wang [a], Fang-Zhou Wang [a], Jun-Song Wang [d], Cheng-Hui Li [a,*], Peng-Fei Zheng [b,*]

[a] State Key Laboratory of Coordination Chemistry, School of Chemistry and Chemical Engineering, Nanjing National Laboratory of Microstructures, Collaborative Innovation Center of Advanced Microstructures, Nanjing University, Nanjing 210023, PR China
[b] Department of Orthopaedic Surgery, Children's Hospital of Nanjing Medical University, Nanjing 210000, Jiangsu Province, PR China
[c] Shanghai Key Laboratory of Orthopaedic Implant, Department of Orthopaedic Surgery, Shanghai Ninth People's Hospital, Shanghai Jiao Tong University School of Medicine, Shanghai 200011, PR China
[d] School of Environmental and Biological Engineering, Nanjing University of Science and Technology, Nanjing 210014, Jiangsu Province, PR China

ARTICLE INFO

Keywords:
3D printing
Hydrogel
DLP
Wound healing
Blue light

ABSTRACT

3D printing hydrogels are widely used in biomedicine because of their unique flexibility, water richness, biocompatibility, and most importantly, the ability to manufacture customized complex structures. Among the various 3D printing technologies for hydrogels, Digital Light Processing (DLP) is advantageous due to its fast speed and high precision. However, the high-energy ultraviolet (UV) light used in most DLP can damage the biomaterials, which limits their application in biomedicine. Herein, by introduction of multiple strengthening mechanisms (nanofibers, hydrogen bonds and coordination bonds) and double photo-initiators, we designed a 2-acrylamide-2-methyl-propanesulfonic acid (AMPS)-based hydrogel, which can be manufactured into various high-precision structures through 3D printing with blue light (450 nm). The printed hydrogel has good mechanical properties, high water absorption capacity, and strong water retention property. Vitro and *in vivo* experiments revealed that the printed hydrogels show excellent biocompatibility, hemostasis effect and antibacterial properties. We further expand the application of 3D printing in the field of precision medicine. The use of 3D printed hydrogels can achieve accurate fitting and wound repair according to the structure of the patient's wound, providing better curative effect to the patient.

1. Introduction

Hydrogel is a kind of polymer material composed of hydrophilic polymer network and a large amount of water. Because of its good biocompatibility, reversible large deformation and intelligent responsiveness to various chemical or physical stimuli, hydrogel is widely used in many fields, including biomedicine [1–5], pharmacy [6–10], flexible electronics [11–16], environmental engineering [17,18] and other fields [19,20]. Especially in the field of biomedicine, hydrogels have unique applications, such as wound dressings [21,22], cell cultures [23,24] and tissue reconstruction [25]. Many researchers have even begun to study artificial biological organs based on hydrogels [26]. The traditional hydrogel production process is cast forming. Therefore, only two-dimensional or simple three-dimensional structures can be made, which greatly limits the application of hydrogels. To address this concern, three-dimensional (3D) printing has been proposed for hydrogel manufacture [27–29]. As compared to cast forming, 3D Printing has various advantages such as short manufacturing cycle, complex structure forming, material saving and energy saving. More importantly, 3D Printing can break through the limitations of traditional parts in appearance design and processing technology, theoretically can produce objects of any shape [30,31].

3D printing for hydrogels mainly include direct ink writing (DIW) [32,33], digital light processing (DLP) [34,35], Stereo lithography Appearance (SLA) [36], volumetric additive manufacturing (VAM) [37], and Two-photon polymerization (TPP) [38,39]. Among them, DLP

* Corresponding authors.
E-mail addresses: dg20240031@smail.nju.edu.cn (X.-C. He), lyh19950227sjtu@sjtu.edu.cn (Y.-H. Liu), chli@nju.edu.cn (C.-H. Li), zhengpengfei@njmu.edu.cn (P.-F. Zheng).
[1] These authors contribute equally to this work.

https://doi.org/10.1016/j.cej.2024.152439
Received 6 March 2024; Received in revised form 27 April 2024; Accepted 20 May 2024
Available online 23 May 2024

technology is advantageous due to its fast speed and high precision. But printing the same model by DLP requires more materials to prepare than DIW. Ultraviolet (UV) light is the common light source for DLP technology, as UV light can ensure rapid polymerization and correspondingly short build times (usually only takes a few seconds) [40,41]. However, the high energy of UV radiation will cause damage to biological tissues, organs, and the loaded cells [42]. In addition, some functional additives such as TiO_2 and SiO_2 nano-particle will absorb light with wavelengths below 400 nm, thus will hinder the polymerization of traditional hydrogels triggered by ultraviolet light [43]. Therefore, using blue light instead of UV light in 3D printing is highly desirable [44], especially when precision medicine based on 3D printing technology has been more and more important in these days. However, there are two main challenges to be addressed for realizing blue light 3D printing of hydrogels. The first is how to achieve good hydrogel-forming ability when it contains a lot of water. Another is how to obtain a photoinitiator system that is sensitive to blue light and can effectively initiate optical crosslinking even in low-energy and water environments. J. Shao reported a blue-light printed hydrogel via extrusion-based printing and post-blue light crosslinking combined process. This method is cumbersome, and can not meet the printing of models with complex internal structure [45]. So far, blue light 3D printable hydrogels have rarely been reported.

In this work, by introduction of nanofibers, hydrogen bonds and coordination bonds, hydrogels with high mechanical strength and interlayer stacking ability are prepared. Through the combination of aqueous initiators 2,4,6-trimethyl-benzoyl-phenyl-phosphine ethyl ester (TPO-L) and phenyl-2,4,6-trimethyl-benzoyl-phosphine lithium (LAP), we have obtained a composite initiator that can effectively initiate radical polymerization in the wavelength range from 280 nm to 600 nm. The absorption intensity in blue light (420–450 nm) is sufficient to support 3D printing. As shown in Fig. 1, this hydrogel can construct various complex structures through blue-light 3D printing, and has excellent antibacterial activity, cytocompatibility, as well as hemostasis properties. We further expand the application of 3D printing in the field of precision medicine. Through high-precision 3D printing, accurate fitting hydrogels can be provided to each case according to the structure of the patient's wound, and the wound healing efficiency can be improved. The hydrogels designed in this work may also have high application potential in drug delivery, tissue engineering, flexible electronic, soft robot, environmental engineering and other fields.

2. Results and discussion

2.1. Hydrogel scaffold with high mechanical strength

Most hydrogels are wet and soft, thus cannot maintain their shape even without loading, which is unfavorable for 3D printing. To develop blue light 3D printable hydrogels, the first challenge to be addressed is to achieve good mechanical strength in photo-curing hydrogels. In the literature, introducing nanocomposite as fillers have been proven to be effective to enhance the mechanical strength of hydrogels [46]. In these nanocomposite reinforced hydrogels, covalent bonding or non-covalent interactions (such as ionic interaction, hydrophobic interaction, and hydrogen bonding) were incorporated at the interface to improve the compatibility between the fillers and the matrices [47]. Based on these studies, we choose the sodium salt of 2-acrylamido-2-methylpropane sulfonic acid (AMPS-Na) as the hydrogel backbone, carboxymethyl cellulose (CMC) as the nanofibers, and introduce hydrogen bonds and coordination bonds to achieve hydrogels with high mechanical properties and interlayer stacking ability. The chemical formula of main composition is shown in Fig. 2**a**.

Synthetic hydrogels based on AMPS-Na has already attracted intense interest in recently years. The advantages of these synthetic hydrogels are that they are soft, flexible, and importantly, any residual unreacted monomer can be more easily removed by water as the polymerization was performed in an aqueous system. Moreover, The AMPS-Na exhibits double electric layer in aqueous solution as shown in Fig. 2**b**. Due to the migration of Na^+ under the action of water molecules, the negative charge of AMPS molecular chains repels each other, and more water

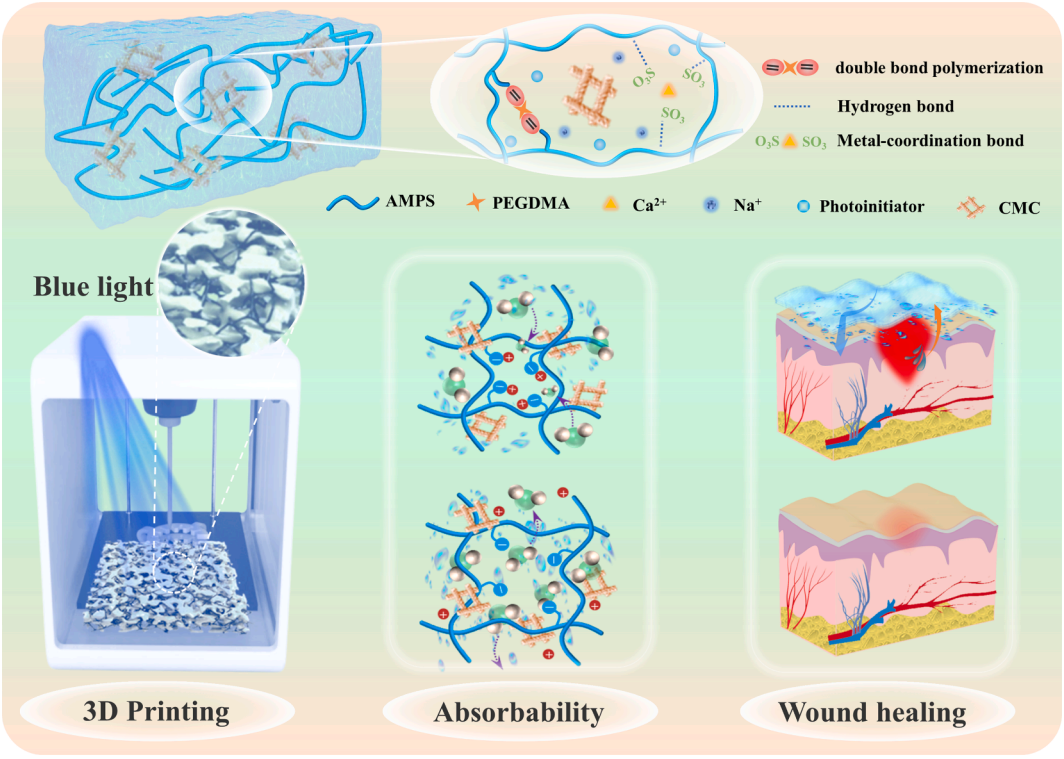

Fig. 1. Schematic diagram of blue light 3D printing hydrogel and its application. (For interpretation of the references to colour in this figure legend, the reader is referred to the web version of this article.)

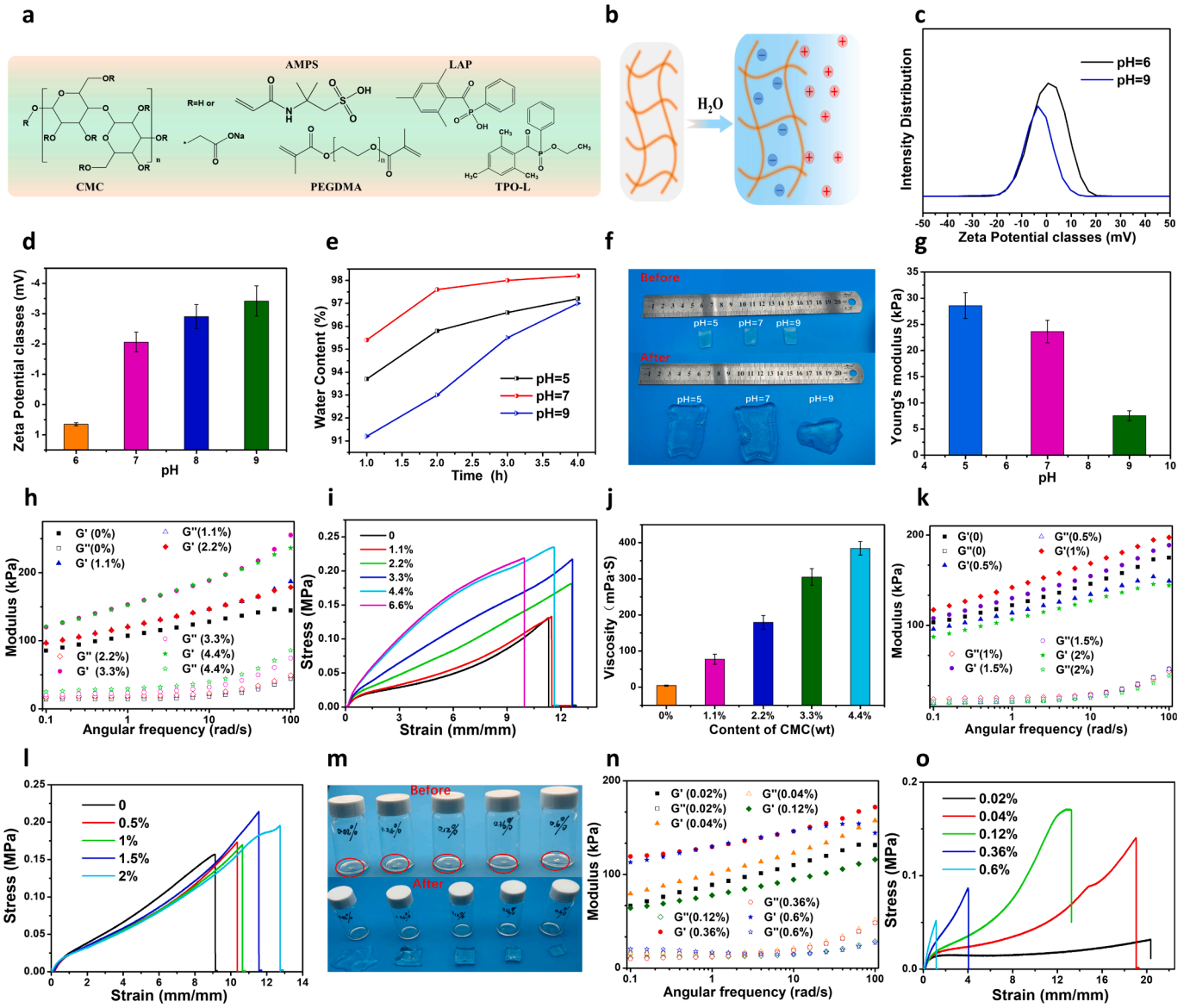

Fig. 2. Design and characterization of the hydrogel scaffold. **(a)** Chemical formula of main ingredients of the hydrogel. **(b)** Under the action of water molecules, AMPS molecular chains repel each other due to the negative charge. **(c)** Distribution curve of zeta potential in AMPS solution at pH values of 6 and 9. **(d)** Relationship between zeta potential and pH value of AMPS solution. **(e)** Comparison of water absorption of hydrogels with different pH values and time. **(f)** Comparison of expansion of hydrogels with pH values of 5,7,9 after soaking in deionized water for 1 h. **(g)** The relationship between pH value and modulus of AMPS hydrogels. **(h).** Dynamic frequency scanning was performed at 0.1 ~ 100 Hz for different CMC addition amount. **(i)** The relationship between stress and strain at different CMC addition amounts. **(j)** Viscosity of hydrogels with different CMC ratios. **(k)** Dynamic frequency scanning of hydrogels with 2.2 % CMC and different $CaCl_2$ ratios at 0.1 ~ 100 Hz. **(l)** Strain-stress curves of hydrogels with 2.2 % CMC and different $CaCl_2$ ratios. **(m)** Comparison of morphology before and after 1 h water absorption. **(n)** Dynamic frequency scanning of hydrogels with 2.2 % CMC, 0.5 % $CaCl_2$ and different PEGDMA ratios. **(o)** Strain-stress curves of hydrogels with 2.2 % CMC, 0.5 % $CaCl_2$ and different PEGDMA ratios.

molecules penetrate into the polymer network due to negative pressure. As evidenced by the shift in the zeta potential, the AMPS molecular chain carries more and more negative charge when the pH value increases (Fig. 2**c**, Fig. 2**d**, and **Fig. S1**). Therefore, high pH is favorable for water absorption. It was found that when pH increased from 5 to 7, the water absorption capacity increased significantly. However, when the pH is further increased, the water absorption capacity decreases (Fig. 2**e**, Fig. 2**f**). This is because the crosslinking degree of photocuring will decrease due to the obstructive effect of hydroxide on free radical polymerization at high pH, resulting in a lower modulus (Fig. 2**g**). On the contrary, at low pH, the AMPS aqueous solution is more prone to free polymerization, resulting in unstable solution (**Fig. S2**). Upon comprehensive consideration, pH of 7 ~ 7.5 was selected as the best option.

Various additives were then introduced to further strengthen the hydrogel. First, CMC was introduced because CMC can form a large number of hydrogen bonds with AMPS and water molecules, and function as a nano-fiber to strengthen the hydrogel. On the other hand, CMC has antibacterial property [48–50] and hemostasis ability, [51–53] which are favorable for wound healing. As shown in Fig. 2**h** and Fig. 2**i**, the modulus and tensile strength of the hydrogel continues to increase with the increase of CMC dosage. Meanwhile, a higher amount (less than 3.3 %) of CMC is beneficial to mechanical strength, but too much filling (more than 4.4 %) will lead to the decrease of elongation at break which will reduce the toughness of the hydrogel. Compared with 4.4 % CMC, the elongation at break of 6.6 % CMC decreased from 1165 % to 997 %, and the toughness decreased from 1.69 MJ/m^3 to 1.36 MJ/m^3. Excess CMC resulted in the increase of the viscosity of AMPS solution which is unfavorable for 3D printing (Fig. 2**j**). Ca^{2+} was also introduced into the

hydrogel as it can form coordination bond with sulfonic acid groups from AMPS and carboxylate groups from CMC, thus can improve the compatibility between the fillers and the matrices. Moreover, Ca^{2+} can promote cell growth and blood coagulation [54–56]. As shown in Fig. 2**k** and Fig. 2**l**, the strength is the highest when the addition amount of $CaCl_2{\cdot}2H_2O$ is 1.5 %. Further increasing the addition amount of $CaCl_2$ will reduce the strength due to the adverse effects of excess $CaCl_2$ on polymerization, and the hydrogel will become sticky and soft. Finally, polyethylene glycol dimethacrylate (PEGDMA)with M_W of 600 was introduced to increase the crosslinking density [57,58]. As shown in Fig. 2**m,** when the amount of PEGDMA is lower than 0.04 %, the hydrogel cannot maintain the three-dimensional shape. Higher amount of PEGDMA leads to more crosslinking points, thus more robust three-dimensional network can be obtained (Fig. 2**n** and Fig. 2**o**). However, high crosslinking degree will restrain the molecular chain migration and inhibit water molecules to enter, thus making the hydrogel brittle and reducing the water absorption capacity. Based on the above considerations, the optimal ratio for these additives are CMC 2.2 %, $CaCl_2{\cdot}2H_2O$ 0.5 % and PEGDMA 0.12 %.

2.2. Blue light 3D printing with double component photo-initiator

The second challenge to be addressed for developing blue light 3D printable hydrogels is to obtain an initiation system that is sensitive to blue light and can effectively initiate optical crosslinking even in low-energy environments.

We first choose TPO-L as the photo-initiator of hydrogels, because this initiator exhibits absorption in the blue light region **(**Fig. 3**a)** and has good solubility in water environment **(Fig. S3)**. However, the blue light response of TPO-L initiated hydrogel is very slow. The viscosity starts to increase after 20 s **(**Fig. 3**b)** of irradiation (exposure energy of 6 mW/cm^2). Such speed is not conducive to 3D printing. It is indeed

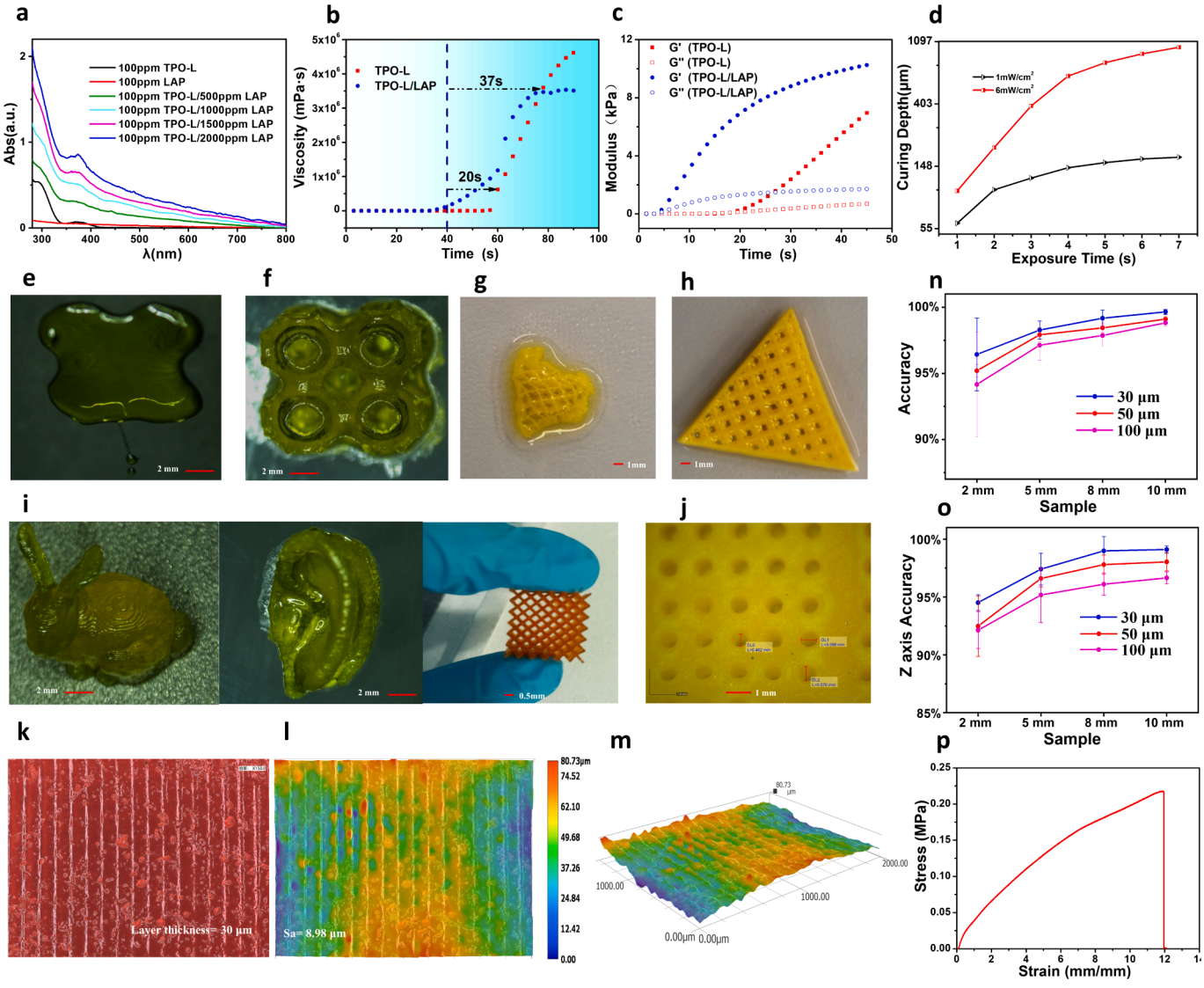

Fig. 3. Blue light 3D printing with double component photo-initiator. **(a)** Ultraviolet absorption spectra of Top-L and TPO-L/LAP mixed initiators. **(b)** Changes in viscosity of hydrogels using TPO-L and TPO-L/LAP as initiators under blue light irradiation at different times. **(c)** Photorheology of hydrogels using TPO-L and TPO-L/LAP as initiators. **(d)** Relationship between curing depth and exposure time at exposure energies of 1 mW/cm^2 and 6 mW/cm^2, respectively. **(e)** Photograph of 3D printed hydrogel prepared with pure AMPS. **(f)** 3D printed AMPS hydrogel strengthened by CMC and $CaCl_2{\cdot}2H_2O$. **(g)** Hydrogel printed with TPO-L as initiators. **(h)** Hydrogel printed with TPO-L-LAP as initiators. **(i)** Various 3D printed hydrogel objects. **(j)** Aperture testing of the 3D printed hydrogel. **(k)** Roughness test (layer thickness 30 μm) of the 3D printed hydrogel. **(l)** Top view of the surface of 3D printed hydrogel. **(m)** Surface stereogram of the 3D printed hydrogel. **(n)** Precision characterization at X/Y-axis. **(o)** Precision characterization at Z-axis. **(p)** Tensile strength test of 3D printed hydrogels. (For interpretation of the references to colour in this figure legend, the reader is referred to the web version of this article.)

possible to improve the light response by increasing the light intensity and extending the exposure time. However, with high light intensity and long exposure time, the peripheral light in 3D printing may cause the resin outside the print layer to cure, resulting in printing failure or affecting the accuracy. We therefore add another photo-initiator LAP into the system as LAP has a wide absorption range (Fig. S4) and double component photo-initiator system has been proven to be efficient in improving photo-initiation rate [59,60]. As shown in Fig. 3**a, a** double-component initiator with good absorption ability in a wide wavelength range was obtained through combining TPO-L with LAP with the weight

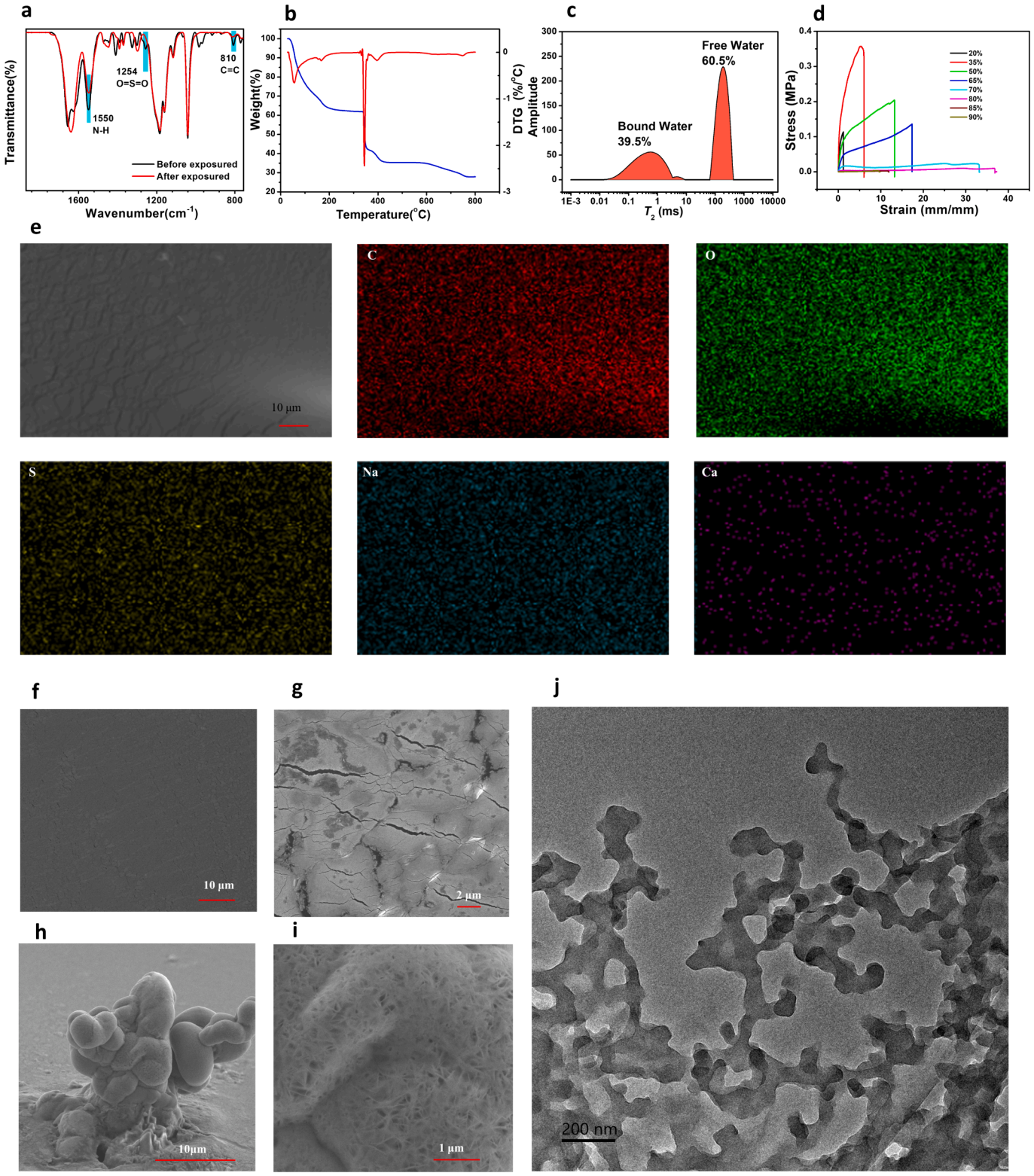

Fig. 4. General characterization and anti-freezing effect of the 3D printed hydrogel. **(a)** FT-IR spectra of hydrogel before and after exposure. **(b)** TGA and DTG curves of the hydrogel. **(c)** Low-field ^{1}H NMR spectrum of hydrogel. **(d)** Tensile strength under different water content. **(e)** EDS element distribution diagram of hydrogel. **(f)** & **(g)** SEM of the hydrogel surface before and after drying. **(h)** & **(i)** SEM of the fracture surface. **(j)** TEM image of the hydrogel.

ratio of 1:10. The viscosity of TPO-L/LAP system increases rapidly under blue light irradiation (no light was given for the first 40 s, and blue light was only provided afterwards), proving that the reaction has taken place **(**Fig. 3**b)**. After 20 s of irradiation, the viscosity reaches 1.1×10^6 mPa·S. It should be noted that the viscosity of the TPO-L system is even greater than that of the TPO-L/LAP system after 37 s of irradiation. Under blue light irradiation for 5 s, the G' of TPO-LAP system has been significantly greater than G", which proves that it is in solid state. At 20 s, the storage modulus is about 7 kPa **(**Fig. 3**c)** and can meet the supporting conditions of 3D printing. When the exposure energy is 1 mW/cm^2, the curing depth [61] is 0.2 mm at 7 s **(**Fig. 3**d)**. Such low curing depth is not conducive to 3D printing. Upon increasing the exposure energy to 6 mW/cm^2, the curing depth was increased to 1 mm at 7 s, which can ensure good interlayer stack in 3D printing process. However, a large depth may affect the printing accuracy, so in the actual printing process, we usually add a small amount of light blocking agent for adjustment **(Fig. S5)**. Therefore, it is recommended that the minimum energy of the 3D printer is $\geq$ 6 mW/cm^2.

In Fig. 3**e** to Fig. 3**j**, various of dyed blue light 3D printed structural objects are shown. Using ordinary AMPS, the structure cannot be formed (Fig. 3**e**). After adding CMC and $CaCl_2{\cdot}2H_2O$ according to the optimal ratio, the model can be printed readily (Fig. 3**f**). When TPO-L/LAP was replaced by pure TPO, the printed structure was found to be incomplete (Fig. 3**g**). This is due to the insufficient cross-linking degree of TPO initiation hydrogen under blue light. As a comparison, the hydrogen triggered by TPO-L/LAP showed better printing performance (Fig. 3**h**). Fig. 3**i** to Fig. 3**j** show examples of various 3D printed objects, such as rabbit, ear, square hole complex structure and round hole complex structure. The printed structure has high water absorption (**Fig. S6 Fig. S7**). The surface morphology of 3D printed hydrogel samples at a thickness of 30 μm was tested using laser confocal microscopy (Fig. 3**k,** Fig. 3**l, and** Fig. 3**m**). Under the condition of 3D printing with a layer thickness of 30 μm, the surface roughness of the 3D printed hydrogel sample is only 8.98 μm, indicating that the 3D printed sample has a high surface quality. In Fig. 3**n** and Fig. 3**o**, the 3D printing accuracy of 3D printed samples in X-Y horizontal plane and Z-axis direction was tested respectively. The results showed that the 3D printing accuracy was higher under the layer thickness of 30 μm. With the increase of the layer thickness, the 3D printing accuracy in both directions decreases, but even the 2-μm sample printed with the layer thickness of 100 μm has 94.16 % and 92.13 % 3D printing accuracy in the X-Y horizontal plane and the Z-axis direction, respectively. The printed hydrogel has good mechanical properties, shown in Fig. 3**p,** **Fig. S8, Fig. S9, Fig. S10,** with stress at break of 0.22 MPa, elongation of 1187 % and toughness of 1.17 MJ/m^3. Especially, and water absorption increases to 98.96 % from 48.9 % in 24 h. **(Fig. S11).**

2.3. General characterization and anti-freezing effect

The FT-IR spectra of hydrogel before and after polymerization were shown in Fig. 4**a**. After radical polymerization triggered by blue light exposure, the absorption band at 810 cm^{-1} which was related to the C = C twisting vibration of the acrylate groups [62] decreased significantly, indicating that cross-linking reaction have taken place. The peak at 1550 cm^{-1} for the bending vibration of N–H became lower after exposure, which means that the N–H bond are restrained to a certain extent after crosslinking. The peak at 1254 cm^{-1} is for the antisymmetric stretching vibration of O = S = O decreased significantly after exposure, indicating that the vibration of sulfonic acid root is greatly restrained after cross-linking.

In the TG-DTG diagram as shown in Fig. 4**b**, the weight loss is about 25 % at 100 °C, which is mainly due to the evaporation of water. The sudden drop at about 350 °C should be due to the polymer degradation [63]. However, in fact, there is about 48.9 % water in the 3D printed hydrogel. The water in hydrogels can be divided into two types, one is free water, the other is bound water [64]. In order to distinguish the different states of water in hydrogels, we performed the Low-field ^{1}H NMR spectrum test (Fig. 4**c**). The results show that 60.5 % of the water in hydrogel is free water, and 39.5 % is bound water. The introduced $CaCl_2$ can coordinate with trapped water to improve water retention ability [64] (**Fig. S12**). The water content has an important effect on the strength of hydrogels, As show in Fig. 4**d**, since the water content increases from 35 % to 80 %, the strength continuously decreases and the elongation at break continuously increases. When the moisture content achieves 80 %, the elongation at break is over 3600 %. This is because as the water content increases, the flexible molecular chains continue to stretch, and the physical crosslinking density continues to decrease, resulting in a continuous decrease in modulus. When the water content further increases, the low crosslinking density results in almost loss of tensile strength. When the water content is lower than 35 %, continue to reduce the water content, the molecular chain of the hydrogel cannot be unfolded, and the winding and force of the molecular chain are lost, resulting in a sharp decline in strength and elongation at break.

It also could be seen from the EDS diagram that C, O, S, Na, Ca and other elements are uniformly distributed in the hydrogel (consistent with **Fig. S13**), and the content of Ca ion is relatively low (Fig. 4**e**). According to the SEM of hydrogel surface, the cured surface of hydrogel is relatively flat, and the surface has tiny cracks after drying (Fig. 4**f**, Fig. 4**g**). The prominent structure on the fracture surface of hydrogels was observed, which may be caused by CMC filling (Fig. 4**h**). It is the reason for the high elongation at break and tensile strength, and it helps with the molding capabilities of 3D printing. We also observed the porous structure, which may be caused by the drying method. (Fig. 4**i**). It can be seen from TEM that the introduced CMC and $CaCl_2$ interacted in the hydrogel to form a complex network (Fig. 4**j**). This network structure improves the mechanical properties of the hydrogels, especially the ability to stack and form between layers during 3D printing. These results show that the prepared hydrogels were homogeneous and stable, without precipitation, caking or equal division.

2.4. Biocompatibility, hemostasis effect and antibacterial property

The hydrogel's biological functions were then evaluated by *in vitro* and *in vivo* experiments. The effects of hydrogel on HUVECs (Human Umbilical Vein Endothelial Cells) were first tested to investigate its biocompatibility. As shown in Fig. 5**a**, different concentration of $CaCl_2$ was tested by cck-8 assay. The results indicate that concentration lower than 16 mg/ml of $CaCl_2$ have good cytocompatibility and even promote the cell proliferation (8–2048 μg/ml). Therefore, the concentration of $CaCl_2$ added in hydrogel (5 μg/ml) is in the safe range. Then, the cytocompatibility of hydrogel was verified by both cck-8 and live/dead staining assay. The results show that HUVECs could adhere to the surface of hydrogel and remain a high viability during 5 days' test (Fig. 5**b & 5c**), which can support cells proliferation in wound healing process. In addition, we have tested the cell viability after irradiating 2 min by blue (450 nm, 4.25 W/cm^2) and UV (365 nm, 4.25 W/cm^2) light, and found that blue light has better cytocompatibility than UV light. In fact, blue light shows no significant difference with control group without light irradiation (Fig. 5**d**). These results underline the necessity to use blue light in 3D printing of biomedical materials.

Antibacterial property is also important in wound healing as the environment of wound is usually dirty in practice. In our hydrogel system, the negative charge of AMPS molecular chains also repels the negative charged membrane of bacteria, which could reduce bacterial adherence. To evaluate the antibacterial efficacy, gram-positive (*S. aureus*, MRSA) and −negative (*E. coli*) bacteria were seeded on the surface of hydrogel. As shown in Fig. 5**e**, there was almost no colony appearance in the agar plates after 6 h coculture with hydrogel in *E. coli*. And the colony appearances of positive bacteria (*S. aureus*, MRSA) were both declined significantly. Further quantitative experiment indicated that the antibacterial rates of hydrogel were 99.96 %, 99.92 % and 99.93 % for *S. aureus, E. coli,* and MRSA, respectively (Fig. 5**f**). The

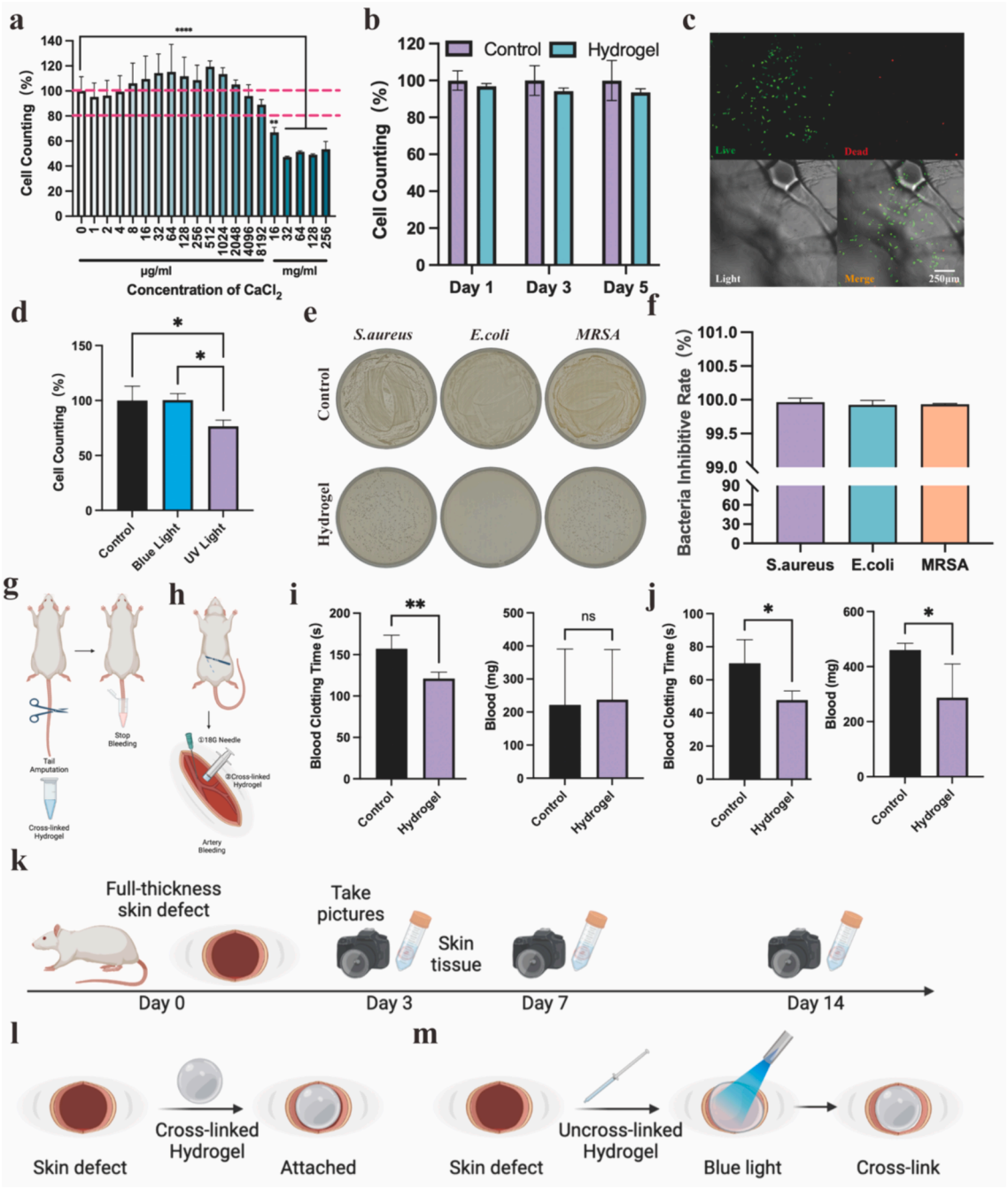

Fig. 5. Biocompatibility, hemostasis effect and antibacterial property of the 3D printed hydrogel. **(a)** cck-8 tests of HUVECs with different concentration of $CaCl_2$. **(b)** cck-8 test of HUVECs cocultured with hydrogel. **(c)** Live/dead staining picture of HUVECs on hydrogel at day 3. **(d)** cck-8 tests of HUVECs with blue and UV light irradiated. **(e)** Bacteria survivor resuspending solution on agar plate after 6 h. **(f)** Statistical results of antibacterial rate. **(g)** & **(h)** Schematic illustration of rat-tail amputation and rat femoral artery injury model. **(i)** Statistical results of blood clotting time and blood loss for rat-tail amputation. **(j)** Blood clotting time and blood loss for rat femoral artery injury. **(k)- (m)** Schematic illustration of full thickness skin defect model. (For interpretation of the references to colour in this figure legend, the reader is referred to the web version of this article.)

excellent antibacterial ability of the hydrogel could protect the wound area from infection in practice application.

As the hemostasis is the first stage of wound healing, the pro-coagulation performance of the samples was tested directly *in vivo*. Rat-tail amputation and rat femoral artery injury model were both assessed (Fig. 5**g & 5h**). For rat-tail amputation, the blood clotting time was shortened using hydrogel compared with control, but the blood loss weight had no significant difference between the two groups (Fig. 5**i**). For rat femoral artery injury, hydrogel application indicated shorter blood clotting time and less blood loss than control group (Fig. 5**j**). Comprehensively, the hydrogel has effective hemostasis ability *in vivo*. The hemostatic performance is mainly originated from two aspects: 1) Ca^{2+} added in hydrogel could accelerate blood clotting [54–56]. 2) According to previous studies, the great water absorption ability could also promote the hemostasis process [65,66].

2.5. Wound healing performance

Full thickness skin defect model was made to evaluate the wound healing performance and antibacterial ability of the hydrogel *in vivo*. In

order to demonstrate the advantage of 3D printing for precision medicine, the hydrogels were divided into pre-crosslinked group and in-situ crosslinked group for infected wound treatment while using standard gauze with or without bacteria as infected and uninfected control (Fig. 5**k-m**). The pre-crosslinked hydrogel were prepared by 3D printing to fit the shape of defect area, while the in-situ crosslinked group were prepared by irradiating the hydrogel dropped onto the defect area. Both the 3D printing and in-situ crosslinked groups have excellent performance to fit and attach to defect area (**Fig. S14**). However, due to the exudation and bleeding from the wound area, it was difficult to crosslink the hydrogel in situ without cleaning the liquid which could dilute the concentration of hydrogel. On the contrary, pre-crosslinked 3D printing hydrogel were more convenient and efficient when attached to the wound area.

As shown in Fig. 6**a-c**, groups treated with hydrogels closed faster than both infected and uninfected controls, especially in the early stage. Besides, in-situ crosslinked hydrogel group showed a smaller wound area than other groups. Close rates of all groups were increased on day 7, and eventually all the wound area closed at day 14. Particularly, infected group did not heal as well as other groups. The results indicated that the hydrogel could accelerate the wound healing process and make wound heal like uninfected, better than the defect under infected condition without treat. Benefit from the ability to accelerate clotting, the first of wound healing, in-situ crosslinked and pre-crosslinked hydrogel groups had better performance in early stage.

For further observation of wound healing, histomorphology analysis has also been adopted. In H & E staining pictures (Fig. 6**d**), all groups appeared the same trends as general observation and close rate changes. At day 3 and 7, infected group neutrophil infiltration than other groups, which caused by the residual bacteria in defect area detected by Giemsa

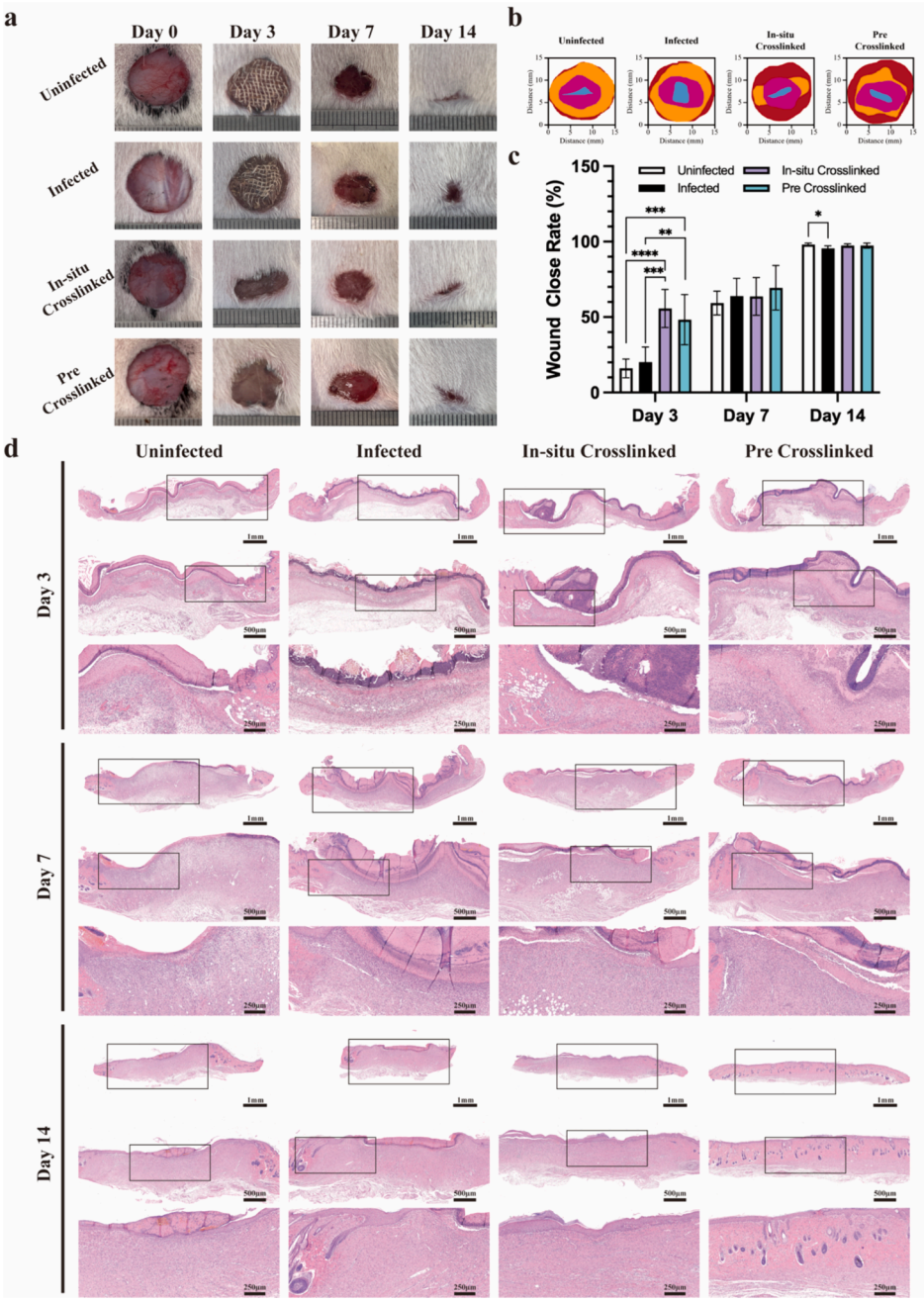

Fig. 6. Wound healing performance of the 3D printed hydrogel. **(a)** & **(b)** Images of wound treated by samples on 0, 3, 7 and 14 days. **(c)** Quantification of wound close rate. **(d)** H&E staining of wound tissue at set time points.

staining (Fig. S15). And at day 14, hydrogels groups showed complete epithelial and structures while infected and uninfected groups were not complete entirely. Collagen filling was observed in all groups by Masson staining (Fig. S16**a**). In hydrogels groups, collagen filling was more remarkable than control groups, especially at day 3 and 7. In addition, the immunohistochemistry staining of IL-6 (Fig. S16**b**), the typical proinflammatory cytokines, showed IL-6 increased from 3 to 7 days and decreased from 7 to 14 days in uninfected control, in-situ crosslinked and pre-crosslinked groups. In infected group, IL-6 did not decrease at 14 days, which could explain why the close rate of infected group was higher than uninfected group at day 3 and 7, but lower at the end. IL-6 has the function of improve vascularization and collagen deposition that accelerate wound healing, but prolonged IL-6 stimulation caused by bacteria could result in non-healing wound [67,68]. All the above results demonstrated that the hydrogel had the characteristic of accelerate wound healing either in-situ or pre-crosslinked. The great wound healing abilities of the hydrogel could be attributed to the following aspects: excellent biocompatibility promote cell proliferation for wound healing. Great water absorption removes the excess exudate of wound area [35], keeps the environment moist and combined with the introduced Ca^{2+} brings great hemostasis properties. Additionally, high antibacterial rate protects the wound area from infection and persistent inflammation.

3. Conclusions

In this work, by introduction of multiple strengthening mechanisms (nanofibers, hydrogen bonds and coordination bonds) and double photo-initiator, we prepared a hydrogel which supports blue light 3D printing. By converting AMPS into AMPS-Na, an AMPS aqueous solution with a zeta potential of −2.06 mV was obtained. After blue light curing, the water absorption rate increased to 98.96 % from 48.9 % after 24 h. Under the synergistic effect of CMC and Ca^{2+}, the interlayer stacking ability can be improved, thereby achieving high-precision blue light printing. The printed hydrogel has good mechanical properties, with stress at break of 0.22 MPa, elongation of 1187 % and toughness of 1.17 MJ/m^3. Benefit from the Ca^{2+} and CMC, the hydrogel produced great hemostasis and antibacterial properties, as well as excellent biocompatibility. And the combined functions accelerate the wound healing processes. It is worth mentioning that due to the blue-light crosslinking characteristics, the hydrogel can use by both pre-crosslinked like 3D printing and in-situ crosslinked, which broaden the application condition. In emergency condition, uncrosslinked hydrogel can directly fill the defect area and then crosslinked fast to protect the injury tissue from dirty environment, bacteria and accelerate the hemostasis process. When facing irregular tissue defects in surgery, it can also shape up in advance according to the defect shape by 3D printing and precisely fill the wounded part. In addition, both application methods could promote the tissue remodeling. Under the background of precision medicine, we believe that the hydrogel has great potential for wide range clinical applications.

4. Experimental section

4.1. Materials and general characterization

AMPS was purchased from MERYER, NaOH and CMC were purchased from Bide Pharmatech Ltd., TPO-L was purchased from Rhawn, LAP was purchased from Macklin, polyethylene glycol dimethacrylate (PEGDMA) with M_w of 600 was purchased from TCI, $CaCl_2{\cdot}2H_2O$ was purchased from Aladdin. The UV absorption spectrum of initiators was tested by UV-2700 (Shimadzu, Japan). Fourier transform infrared (FT-IR) spectra were measured in a NICOLET IS10 (Thermo Nicolet Co., USA). FT-IR spectrophotometer over the range of 4000–400 cm^{-1}. Zeta potential was tested with Malvern Instruments nanometer size analyzer (model ZS-90). A certain amount of samples was taken and dispersed in deionized water (mass fraction is 0.1 %), ultrasonic oscillation for 3 min. The Zeta potential at different pH values was measured and averaged three times. The optical rheological behavior was tested using the Anton Paar Rotary Rheometer (MCR 502, Austria) with PP-25 (57520) flat panel probe. The test temperature was set at 25 °C, the shear force is 2 Pa/s. A blue light of 450 nm with intensity of 6 mW/cm^2 was applied to simulate the resin crosslinking during the printing process. A DHR-2 Rheometer (TA Instruments) was used to measure the rheological property. A parallel plate (8 mm diameter) was used to measure the frequency sweep curve. Mechanical properties (including tensile stress, ultimate elongation, Young's modulus, compression stress, and so on) were tested on an Instron 3343 Universal Materials Testing Machine (Instron Co., USA). The tensile experiments were carried out on rectangle samples (length 50 mm, thickness 1.0 mm, width of parallel part 2 mm) at a speed of 10 $mm{\cdot}min^{-1}$. Peel strength test was deployed on a texture tester (Leicestershire, UK) equipped with paired longitudinal test fixtures, peel tests are performed at 180° to simulate the adhesion of hydrogels. Low-field ^1H NMR spectrum was measured on a MesoMR23-060H-I NMR analyzer (Suzhou Niumag Analytical Instrument Corporation, China). Unless otherwise specified, material properties were all measured at ambient conditions (RH60 ± 1 %, 25 °C). The thermostabilities of materials were tested on simultaneous thermos-gravimetric analyzer (STA) Netzche STA449F3 (Netzche, Germany) under air atmosphere from 0 °C to 800 °C at a heating rate of 10 °C min^{-1}. XPS was tested on Thermofisher Escalab 250xi, with the 3D printing samples (2 × 2 × 1 cm) dried in 80 °C oven for 12 h. The relatively flat side was selected for test, scanning wavelength at the range of 0 ~ 1200 eV. Step length was set as 0.05 ev, the data corresponding to C, O, Na, Ca and S were collected. SEM adopts S-3400, Hitachi, Japan, TEM adopts JEM-2100plus, Japan, and X-MAX 50 X-ray spectrometer (EDS) from Oxford, UK to observe the microstructure and elementary composition of hydrogels.

4.2. Preparation of 3D printing ink

33 g of AMPS was poured into a flask with 33 g of deionized water. The solution was stirred for 30 min and then titrated with aqueous solution of NaOH to control the PH value between 7.0 and 7.5. $CaCl_2{\cdot}2H_2O$ was then added according to the ratio with stirring for 10 min. Upon heating to 90 °C, CMC was added. After cooling to room temperature after 30 min, a certain amount of TPO-L and LAP was added with stirring for 30 min. Finally, PEGDMA was added with stirring for 30 min. The prepared material was stored in brown reagent bottle at room temperature and sterilized by filtration using 0.22 μm PES membrane filter unit (Millipore, Ireland) before using.

4.3. 3D printing

The hydrogel is printed by NOVABD device, equipped with blue-ray of 450 nm and intensity of 6 mW/cm^2. The printing layer thickness is 30 μm. Exposure time is 10–30 s. Printing accuracy is defined as the ratio between the actual size and the size of the design model. According to the following formula, where P_p is the actual size and P_d is the design size.

$$P = \frac{P_p}{P_d} \tag{1}$$

Roughness was test on VHX-7000N (KEYENCE, Japan). The sample is placed on the stage, the camera lens and the stage are adjusted, the test point is initially found, the focus knob is rotated until the clear image is obtained and the depth 3D topography is synthesized. At the same time, the output arithmetical mean height (Sa) indicates the surface roughness.

4.4. Determination of swelling ratio and dehydration ratio

The water contents of the hydrogels were measured using the weight

change upon vacuum freeze dehydration. The water content C (wt) is defined by the weight of hydrogels after lyophilization (W_1) and the total weight of the hydrogels before lyophilization (W_0), and calculated using the following equation:

$$C(\mathrm{wt}) = \frac{W_0 - W_1}{W_0} \times 100\% \quad (2)$$

The water absorption ratio of hydrogels was tested by the weight change before and after swelling. The swelling ratio was calculated using the following equation, where the W_s is the weight of the hydrogels after swelling, and the W_0 is the weight of the hydrogels before swelling.

$$S(\mathrm{wt}) = \frac{W_s - W_0}{W_0} \times 100\% \quad (3)$$

The dehydration ratio of hydrogels was tested by the weight change before and after heated in a vacuum oven at 80 °C. W_0 is the weight of the hydrogels before dehydrated, and W_d is the weight after dehydrated. The dehydration ratio was calculated using the following equation:

$$D(wt) = \frac{W_0 - W_d}{W_0} \times 100\% \quad (4)$$

For freeze–thaw cycle test, the printed hydrogel was frozen at −20 °C for 1 day, and then thawed at 25 °C for 2 days for a cycle. A total process contained 3 cycles.

4.5. Cytocompatibility test

The cytocompatibility of $CaCl_2$ and hydrogel samples was tested by cck-8 assay by using HUVEC (Human Umbilical Vein Endothelial Cells) as model cells. Briefly, the cells were planted in 96-well plate for 24 h with DMEM (10 % FBS). Then, different concentration of $CaCl_2$ were added and co-cultured with HUVEC for another 24 h. The samples were rinsed with sterilized PBS for three time and the cell viability was assessed via cck-8 by detecting the optical density at 450 nm using a microplate reader (Infinite M200 pro, Tecan). As for the hydrogel samples, cells were directly seeded on the samples and tested after 24 h' co-culture by the same method. The morphologies of HUVEC seeded on hydrogels for 24 h were directly detected by live/dead staining assay and capturing with confocal microscope (Leica Microsystems Inc., USA).

4.6. Antibacterial performance test

Gram-positive *Staphylococcus aureus* (*S. aureus*, ATCC 25923), *Methicillin-resistant Staphylococcus aureus* (MRSA, ATCC 43300) and gram-negative *Escherichia coli* (*E. coli,* ATCC 25922) were used for test antibacterial performance of hydrogels. And LB liquid medium and nutrient agar plates are used for culture bacteria. 10 μL of 10^7 CFU/mL bacterial solution was seeded on the surface of 10 mg sterilized hydrogel samples and use 10 μL alone as control. After incubation at 37 ℃ for 6 h, 990 μL of sterilized PBS was added in each group for suspending bacteria. Dilution plating procedure was adopted to observe the antibacterial performance and calculate the antibacterial rate.

4.7. Animal experiments

24 SD rats (~300 g) were randomly assigned to Control and hydrogel groups. The rats were feed with sufficient water and abrosia for 12 h. Each rat's tail was cut in the middle and free bleed for 30 s after anesthetized. After that, filter paper and hydrogels were used to treated control and hydrogel groups, respectively, the blood clotting time and blood loss weight were record. As well, rat femoral artery injury was operated for another model. In brief, the blood clotting time and blood loss weight were record after femoral artery injury was created by an 18 G needle. 18 SD rats (~300 g) were sacrificed for implemented full thickness wound healing experiments. On the dorsal of rats, four 10 mm round full thickness skin defects were cut after anesthetized by 3 % (w/v) pentobarbital sodium by intraperitoneal injection. Each defect was treated with different materials: 1) Control group: sterile gauze; 2) Infected group: gauze with bacteria solution; 3) In-situ crosslinked group: hydrogel crosslinked in defect area with bacteria solution; 4) Pre-crosslinked group: attach the hydrogel crosslinked before the experiment and dropped with bacteria solution. The crosslinked hydrogel groups were both equipped with blue-ray of 450 nm and intensity of 6 mW/cm^2 for 30 s. And the bacteria solution was the mix of *S.aureus* and *E.coli* of 10^7 CFU/mL, and the dropped volume was 20 μL. After treated for 3, 7 and 14 days, the wound area tissue was collected and soaked in 4 % paraformaldehyde solution. Then, the pathological section of wound tissue was stained by H&E, Masson, and Giemsa. In addition, the picture of defects was also taken at each time point to calculate wound healing rate.

All the experimental animals mentioned above were cared for and treated following the NIH guideline for the care and us of laboratory animals (NIH Publication No. 85e23 Rev. 1985). And the animal experiments project was approved by the Research Center for Laboratory Animal of Shanghai Ninth People's Hospital.

4.8. Statistical methods

All data expressed as mean ± standard deviation (SD) was analyzed using SPSS 15.0. One-way analysis of variance (ANOVA) and student *t*-test was used for comparison. Comparisons with *p < 0.05, **p < 0.01, ***p < 0.001, and ****p < 0.0001 were considered statistically significant.

CRediT authorship contribution statement

Xiu-Chong He: Writing – original draft, Methodology, Formal analysis, Data curation. **Xiu-Ning Chen:** Writing – original draft, Methodology, Formal analysis, Data curation. **Yi-Hao Liu:** Methodology, Investigation, Formal analysis. **Xinyu Zhong:** Methodology, Investigation. **Lei Qiang:** Methodology, Investigation. **Hong-Qin Wang:** Software, Formal analysis. **Fang-Zhou Wang:** Methodology, Investigation. **Jun-Song Wang:** Software, Methodology. **Cheng-Hui Li:** Writing – review & editing, Supervision, Conceptualization. **Peng-Fei Zheng:** Writing – review & editing, Supervision, Conceptualization.

Declaration of competing interest

The authors declare that they have no known competing financial interests or personal relationships that could have appeared to influence the work reported in this paper.

Data availability

Data will be made available on request.

Acknowledgements

Fig. 5**. g, h, k, l**, and **m** were created with biorender.com. This work was supported by the National Natural Science Foundation of China (Grant No. 22271139), the Fundamental Research Funds for the Central Universities (020514380281), China Postdoctoral Science Foundation (2022M721685) and China Postdoctoral Science Foundation Special Grant Program (2023T160331).

Appendix A. Supplementary data

Supplementary data to this article can be found online at https://doi.org/10.1016/j.cej.2024.152439.

References

[1] I. Tomatsu, K. Peng, A. Kros, Photoresponsive hydrogels for biomedical applications, Adv. Drug Delivery Rev. 63 (14–15) (2011) 1257–1266, https://doi.org/10.1016/j.addr.2011.06.009.

[2] A.S. Hoffman, Hydrogels for biomedical applications, Adv. Drug Delivery Rev. 54 (1) (2002) 3–12, https://doi.org/10.1016/S0169-409X(01)00239-3.

[3] S. Correa, A.K. Grosskopf, H.L. Hermandez, D. Chan, A.C. Yu, L.M. Stapleton, E. A. Appel, Translational applications of hydrogels, Chem. Rev. 121 (18) (2021) 11385–11457, https://doi.org/10.1021/acs.chemrev.0c01177.

[4] J. Koehler, F.P. Brandl, A.M. Goepferich, Hydrogel wound dressings for bioactive treatment of acute and chronic wounds, Eur. Polym. J. 100 (2018) 1–11, https://doi.org/10.1016/j.eurpolymj.2017.12.046.

[5] E.M. Ahmed, Hydrogel: Preparation, characterization, and applications: A review, J. Adv. Res. 6 (2) (2015) 105–121, https://doi.org/10.1016/j.jare.2013.07.006.

[6] J. Wang, A. Goyanes, S. Gaisford, A.W. Baist, Stereolithographic (SLA) 3D printing of oral modified-release dosage forms, Int. J. Pharm. 502 (1–2) (2016) 207–212, https://doi.org/10.1016/j.ijpharm.2016.03.016.

[7] T. Tagami, E. Ito, R. Kida, K. Hirose, T. Noda, T. Ozeki, 3D printing of gummy drug formulations composed of gelatin and an HPMC-based hydrogel for pediatric use, Int. J. Pharm. 594 (2021) 120118, https://doi.org/10.1016/j.ijpharm.2020.120118.

[8] H. Herrada-Manchón, D. Rodríguez-González, M.A. Fernández, M. Suñé-Pou, P. Pérez-Lozano, E. García-Montoya, E. Aguilar, 3D printed gummies: Personalized drug dosage in a safe and appealing way, Int. J. Pharm. 587 (2020) 119687, https://doi.org/10.1016/j.ijpharm.2020.119687.

[9] P.R. Martinez, A. Goyanes, A.W. Basit, S. Gaisford, Fabrication of drug-loaded hydrogels with stereolithographic 3D printing, Int. J. Pharm. 532 (1) (2017) 313–317, https://doi.org/10.1016/j.ijpharm.2017.09.003.

[10] Y. Wang, Y. Miao, J. Zhang, J.P. Wu, T.B. Kirk, J. X, D. Ma, W. X, Mater. Sci. Eng.: C 84 (2018) 44–51, https://doi.org/10.1016/j.msec.2017.11.025.

[11] C. Keplinger, J.Y. Sun, C.C. Foo, P. Rothemund, G.M. Whitesides, Z. Suo, Stretchable, transparent, ionic conductors, Science 341 (6149) (2013) 984–987, https://doi.org/10.1126/science.1240228.

[12] C.-C. Kim, H.-H. Lee, K.H. Oh, J.-Y. Sun, Highly stretchable, transparent ionic touch panel, Science 353 (6300) (2016) 682–687, https://doi.org/10.1126/science.aaf8810.

[13] X. Pu, M. Liu, X. Chen, J. Sun, C.D.Y. Zhang, J. Zhai, W. Hu, Z.L. Wang, Ultrastretchable, transparent triboelectric nanogenerator as electronic skin for biomechanical energy harvesting and tactile sensing, Sci. Adv. 3 (5) (2017) e1700015.

[14] Y. Wang, H. Huang, J. Wu. L. Han, Z. Yang, Z. Jiang, R. Wang, Z. Huang, M. Xu, Ultrafast self-healing, reusable, and conductive polysaccharide-based hydrogels for sensitive ionic sensors, ACS Sustainable Chem. Eng. 8 (50) (2020) 18506-18518, 10.1021/acssuschemeng.0c06258.

[15] Z. Lei, Q. Wang, S. Sun, W. Zhu, P. W, A bioinspired mineral hydrogel as a self-healable, mechanically adaptable ionic skin for highly sensitive pressure sensing, Adv. Mater. 29 (22) (2017) 1700321, 10.1002/adma.201700321.

[16] S. Cai, X. Xu, W. Yang, J. Chen, X. Fang, Materials and designs for wearable photodetectors, Adv. Mater. 31 (18) (2019) 1808138, https://doi.org/10.1002/adma.201808138.

[17] Y. Wang, Y. Zhu, Y. Hu, G. Zeng, Y. Zhang, C. Zhang, C. Feng, How to construct DNA hydrogels for environmental applications: advanced water treatment and environmental analysis, Small 14 (17) (2018) 1703305, https://doi.org/10.1002/smll.201703305.

[18] M. Khan, I.M.C. Lo, A holistic review of hydrogel applications in the adsorptive removal of aqueous pollutants: Recent progress, challenges, and perspectives, Water Res. 106 (2016) 259–271, https://doi.org/10.1016/j.watres.2016.10.008.

[19] C. Yang, Z. Suo, Hydrogel ionotronics, Nat. Rev. Mater. 3 (2018) 125–142, https://doi.org/10.1038/s41578-018-0018-7.

[20] Y. Wang, P. Chen, X. Zhou, Y. Liu, N. Wang, C. Gao, Highly sensitive zwitterionic hydrogel sensor for motion and pulse detection with water retention, adhesive, antifreezing, and self-healing properties, ACS Appl. Mater. Interfaces 14 (41) (2022) 47100–47112, https://doi.org/10.1021/acsami.2c14157.

[21] X. Zhao, Y. Liang, Y. Huang, J. He, Y. Han, B. Guo, Physical double-network hydrogel adhesives with rapid shape adaptability, fast self-healing, antioxidant and NIR/pH stimulus-responsiveness for multidrug-resistant bacterial infection and removable wound dressing, Adv. Funct. Mater. 30 (17) (2020) 1910748, https://doi.org/10.1002/adfm.201910748.

[22] J. Zhang, Y. Zheng, J. Lee, J. Hua, S. Li, A. Panchamukhi, J. Yue, X. Gou, Z. Xia, L. Zhu, A pulsatile release platform based on photo-induced imine-crosslinking hydrogel promotes scarless wound healing, Nat. Commun. 12 (2021) 1670, https://doi.org/10.1038/s41467-021-21964-0.

[23] G. Orive, R.M. Hernández, A.R. Gascón, R. Calafiore, T.M.S. Chang, P.D. Vos, G. Hortelano, D. Hunkeler, I. Lacík, A.M.J. Shapiro, J.L. Pedraz, Cell encapsulation: Promise and progress, Nat. Med. 9 (2023) 104–107, https://doi.org/10.1038/nm0103-104.

[24] M. Filipp, B. Dasen, J. Guerrero, F. Garello, G. Isu, G. Born, M. Ehrbar, I. Martin, A. Scherberich, Magnetic nanocomposite hydrogels and static magnetic field stimulate the osteoblastic and vasculogenic profile of adipose-derived cells, Biomaterials 223 (2019) 119468, https://doi.org/10.1016/j.biomaterials.2019.119468.

[25] S. Pina, J.M. Oliveira, R.L. Reis, Natural-based nanocomposites for bone tissue engineering and regenerative medicine: a review, Adv. Mater. 27 (7) (2015) 1143–1169, https://doi.org/10.1002/adma.201403354.

[26] A. Lee, A.R. Hudson, D.J. Shiwarski, J.W. Tashman, T.J. Hinton, S. Yerneni, J. M. Bliley, P.G. Campbell, A.W. Feinberg, 3D bioprinting of collagen to rebuild components of the human heart, Science 365 (6452) (2019) 482–487, https://doi.org/10.1126/science.aav9051.

[27] J.W. Stansbury, M.J. Idacavage, 3D printing with polymers: Challenges among expanding options and opportunities, Dent. Mater. 32 (1) (2016) 54–64, https://doi.org/10.1016/j.dental.2015.09.018.

[28] C. Mendes-Felipe, D. Patrocinio, J.M. Laza, L. Ruiz-Rubio, Evaluation of postcuring process on the thermal and mechanical properties of the Clear02™ resin used in stereolithography, Polym. Test. 72 (2018) 115–121, https://doi.org/10.1016/j.polymertesting.2018.10.018.

[29] S. Gao, Z. Li, S.V. Petegem, J. Ge, S. Goel, J.V. Vas, V. Luzin, Z. Hu, H.L. Seet, D. F. Sanchez, H.V. Swygenhoven, H. Gao, M. Seita, Additive manufacturing of alloys with programmable microstructure and properties, Nat Commun. 14 (2023) 6752, https://doi.org/10.1038/s41467-023-42326-y.

[30] I. Gibson, L.W. Ming, Colour RP, Rapid Prototyp. J. 7 (4) (2001) 212–216, https://doi.org/10.1108/EUM0000000005894.

[31] T.J.K. Buchner, S. Rogler, S. Weirich, Y. Armati, B.G. Cangan, J. Ramos, S. T. Twiddy, D.M. Marini, A. Weber, D. Chen, G. Ellson, J. Jacob, W. Zengerle, D. Katalichenko, C. Keny, W. Matusik, R.K. Katzschmann, Vision-controlled jetting for composite systems and robots, Nature 623 (2023) 522–530, https://doi.org/10.1038/s41586-023-06684-3.

[32] S.Y. Zheng, Y. Shen, F. Zhu, J. Yin, J. Qian, J. Fu, Z.L. Wu, Q. Zheng, Programmed deformations of 3D-printed tough physical hydrogels with high response speed and large output force, Adv. Funct. Mater. 28 (37) (2018) 1803366, https://doi.org/10.1002/adfm.201803366.

[33] C. Du, J. Hu, X. Wu, H. Shi, H.C. Yu, J. Qian, J. Yin, C. Gao, Z.L. Wu, Q. Zheng, 3D printing of a tough double-network hydrogel and its use as a scaffold to construct a tissue-like hydrogel composite, J. Mater. Chem. B 10 (2022) 468–476, https://doi.org/10.1039/D1TB02465E.

[34] S.H. Kim, Y.K. Yeon, J.M. Lee, J.R. Chao, Y.J. Lee, Y.B. Seo, M.T. Sultan, O.J. Lee, J. S. Lee, S.I. Yoon, I.S. Hong, G. Khang, S.J. Lee, J.J. Yoo, C.H. Park, Precisely printable and biocompatible silk fibroin bioink for digital light processing 3D printing, Nat. Commun. 9 (2018) 1620, https://doi.org/10.1038/s41467-018-03759-y.

[35] Y. Hu, H. Tang, N. Xu, X. Kang, W. Wu, C. Shen, J. Lin, Y. Bao, X. Jiang, Z. Luo, Adhesive, flexible, and fast degradable 3D-printed wound dressings with a simple composition, Adv. Healthcare Mate. 13 (3) (2024) 2302063, https://doi.org/10.1002/adhm.202302063.

[36] Y. Bao, N. Paunović, J.-C. Leroux, Challenges and opportunities in 3D printing of biodegradable medical devices by emerging photopolymerization techniques, Adv. Funct. Mate 32 (15) (2022) 2109864, https://doi.org/10.1002/adfm.202109864.

[37] R. Levato, O. Dudaryeva, C.E. Garciamendez-Mijares, B.E. Kirkpatrick, R. Rizzo, J. Schimelman, K.S. Anseth, S. Chen, M. Zenobi-Wong, Y.S. Zhang, Nature Reviews Methods Primers 3 (2023) 47, https://doi.org/10.1038/s43586-023-00231-0.

[38] (G. Lu, R. Tang, J. Nie, X. Zhu, Photocuring 3D printing of hydrogels: techniques, materials, and applications in tissue engineering and flexible devices, Macromol. Rapid Commun., 45 (7) (2024) 2300661, 10.1002/marc.202300661.

[39] F.-C. Bin, M. Guo, T. Li, Y.-C. Zheng, X.-Z. Dong, J. Liu, F. Jin, M.-L. Zheng, Carbazole-based anion ionic water-soluble two-photon initiator for achieving 3D hydrogel structures, Adv. Funct. Mater. 33 (39) (2023) 2300293, https://doi.org/10.1002/adfm.202300293.

[40] H. Ding, M. Dong, Q. Zheng, Z.L. Wu, Digital light processing 3D printing of hydrogels: a minireview, Mol. Syst. Des. Eng. 7 (2022) 1017–1029, https://doi.org/10.1039/D2ME00066K.

[41] H. Li, C. Tan, L. Li, Review of 3D printable hydrogels and constructs, Mater. Des. 159 (2018) 20–38, https://doi.org/10.1016/j.matdes.2018.08.023.

[42] D. Nieto, A. Jorge-Mora, J.A.M. Marchal, L. Moroni, Fundamentals of light-cell–polymer interactions in photo-cross-linking based bioprinting, APL Bioeng. 4 (2020) 041502, https://doi.org/10.1063/5.0022693.

[43] K.J. Cui, C.Z. Zhu, H. Zhang, Q. Xuan, W.Z. Zou, Z.Y. Zhang, X.C. Lin, N. Zhao, J. Xu, Blue laser diode-initiated photosensitive resins for 3D printing, J. Mater. Chem. C 5 (2017) 12035–12038, https://doi.org/10.1039/C7TC04303A.

[44] M. Lee, R. Rizzo, F. Surman, M. Zenobi-Wong, Guiding lights: tissue bioprinting using photoactivated materials, Chem. Rev. 120 (19) (2020) 10950–11027, https://doi.org/10.1021/acs.chemrev.0c00077.

[45] Y. Huang, G. Sun, L. Lyu, Y. Li, D. Li, Q. Fan, J. Yao, J. Shao, Dityrosine-inspired photocrosslinking technique for 3D printing of silk fibroin-based composite hydrogel scaffolds, Soft Matter 18 (2022) 3705–3712, https://doi.org/10.1039/D1SM01817E.

[46] B. Tigges, C. Popescu, O. Weichold, Mechanical and sorption properties of transparent nanocomposite hydrogels, Soft Matter 7 (2011) 5391–5396, https://doi.org/10.1039/C0SM01472A.

[47] A. Kumar, B. Nutan, S.K. Jewrajka, Modulation of properties through covalent bond induced formation of strong ion pairing between polyelectrolytes in injectable conetwork hydrogels, ACS Appl. Bio Mater. 4 (4) (2021) 3374–3387, https://doi.org/10.1021/acsabm.0c01673.

[48] H. Wang, Y. Liu, K. Cai, B. Zhang, S. Tang, W. Zhang, W. Liu, Antibacterial polysaccharide-based hydrogel dressing containing plant essential oil for burn wound healing, Burns Trauma 9 (2021) tkab041, https://doi.org/10.1093/burnst/tkab041.

[49] Q. Zhou, X. Zhou, Z. Mo, Z. Zeng, Z. Wang, Z. Cai, L. Luo, Q. Ding, H. Li, S. Tang, A PEG-CMC-THB-PRTM hydrogel with antibacterial and hemostatic properties for promoting wound healing, Int. J. Biol. Macromol. 224 (2023) 370–379, https://doi.org/10.1016/j.ijbiomac.2022.10.130.

[50] H. Mohammadi, A. Kamkar, A. Misaghi, Nanocomposite films based on CMC, okra mucilage and ZnO nanoparticles: Physico mechanical and antibacterial properties, Carbohydr. Polym. 181 (2018) 351–357, https://doi.org/10.1016/j.carbpol.2017.10.045.
[51] J.-Y. Liu, Y. Li, Y. Hu, G. Cheng, E. Ye, C. Shen, F.-J. Xu, Hemostatic porous sponges of cross-linked hyaluronic acid/cationized dextran by one self-foaming process, Mater. Sci. Eng: C 83 (2018) 160–168, https://doi.org/10.1016/j.msec.2017.10.007.
[52] X. Wang, J. Guan, X. Zhuang, Z. Li, S. Huang, J. Yang, C. Liu, F. Li, F. Tian, J. Wu, Z. Shu, Exploration of blood coagulation of N-alkyl chitosan nanofiber membrane in vitro, Biomacromolecules 19 (3) (2018) 731–739, https://doi.org/10.1021/acs.biomac.7b01492.
[53] S. Cao, Q. Li, S. Zhang, Z. Liu, X. Lv, J. Chen, Preparation of biodegradable carboxymethyl cellulose/dopamine/Ag NPs cryogel for rapid hemostasis and bacteria-infected wound repair, Int. J. Biol. Macromol. 222 (Part A) (2022) 272-284, 10.1016/j.ijbiomac.2022.09.172.
[54] X. Yu, Z. Gao, J. Mu, H. Lian, Z. Meng, Gelatin/calcium chloride electrospun nanofibers for rapid hemostasis, Biomater. Sci. 11 (2023) 2158–2166, https://doi.org/10.1039/D2BM01767A.
[55] A. Kumar, D.K. Sah, K. Khanna, Y. Rai, A.K. Yadav, M.S. Ansari, A.N. Bhatt, A calcium and zinc composite alginate hydrogel for pre-hospital hemostasis and wound care, Carbohydr. Polym. 299 (2023) 120186, https://doi.org/10.1016/j.carbpol.2022.120186.
[56] H. Weng, W. Jia, M. Li, Z. Chen, New injectable chitosan-hyaluronic acid based hydrogels for hemostasis and wound healing, Carbohydr. Polym. 294 (2022) 119767.
[57] H. Li, L. Kuang, J. Li, Y. Zhu, Macromol. Mater. Eng. 306 (2021) 2100588, https://doi.org/10.1002/mame.202100588.
[58] S.N. Anindita, R. Conti, D. Zauchner, N. Paunović, W. Qiu, M.G. Buzhor, A. Krivitsky, Z. Luo, R. Müller, H. Grützmacher, X.-H. Qin, J.-C. Leroux, Y. Bao, Tough PEG-only hydrogels with complex 3D structure enabled by digital light processing of "all-PEG" resins, Aggregate 4 (6) (2023) e368.
[59] Z. Zheng, D. Eglin, M. Alini, G.R. Richards, L. Qin, Y. Lai, Visible light-induced 3D bioprinting technologies and corresponding bioink materials for tissue engineering: a review, Engineering 7 (7) (2021) 966–978, https://doi.org/10.1016/j.eng.2020.05.021.
[60] A. Linnenberger, M.I. Bodine, C. Fiedler, J.J. Roberts, S.C. Skaalure, J.P. Quinn, S. J. Bryant, M. Cole, R.R. Mcleod, Three dimensional live cell lithography, Opt. Express 21 (2013) 10269–10277, https://doi.org/10.1364/oe.21.010269.
[61] M. Sandmeier, N. Paunović, R. Conti, L. Hofmann, J. Wang, Z. Luo, K. Masania, N. Wu, N. Kleger, F.B. Coulter, A.R. Studart, H. Grützmacher, J.-C. Leroux, Y. Bao, Solvent-free three-dimensional printing of biodegradable elastomers using liquid macrophotoinitiators, Macromolecules 54 (17) (2021) 7830–7839, https://doi.org/10.1021/acs.macromol.1c00856.
[62] Y.-J. Park, D.-H. Lim, H.-J. Kim, D.-S. Park, I.-K. Sung, UV-and thermal-curing behaviors of dual-curable adhesives based on epoxy acrylate oligomers, Int. J. Adhes. Adhes. 29 (7) (2009) 710–717, https://doi.org/10.1016/j.ijadhadh.2009.02.001.
[63] J. Yu, Y. Li, Q. Lu, J. Zheng, S. Yang, F. Jin, Q. Wang, W. Yang, Synthesis, characterization and adsorption of cationic dyes by CS/P(AMPS-co-AM) hydrogel initiated by glow-discharge-electrolysis plasma, Iran. Polym. J. 25 (2016) 423–435, https://doi.org/10.1007/s13726-016-0434-8.
[64] J. Wang, B. Wu, P. Wei, S. Sun, P. W, Fatigue-free artificial ionic skin toughened by self-healable elastic nanomesh, Nat. Commun., 13 (2022) 4411, 10.1038/s41467-022-32140-3.
[65] Y. Liu, H. Niu, C. Wang, X. Yang, W. Li, Y. Zhan, X. Ma, Y. Xu, P. Zheng, J. Wang, K. Dai, Bio-inspired, bio-degradable adenosine 5′-diphosphate-modified hyaluronic acid coordinated hydrophobic undecanal-modified chitosan for hemostasis and wound healing, Bioact. Mater. 17 (2022) 162–177, https://doi.org/10.1016/j.bioactmat.2022.01.025.
[66] X. Yang, C. Wang, Y. Liu, H. Niu, W. Zhao, J. Wang, K. Dai, Inherent antibacterial and instant swelling ε-poly-lysine/ poly(ethylene glycol) diglycidyl ether superabsorbent for rapid hemostasis and bacterially infected wound healing, ACS Appl. Mater. Interfaces 13 (31) (2021) 36709–36721, https://doi.org/10.1021/acsami.1c02421.
[67] M.M. Rahman, N. Garcia, Y.S. Loh, D.C. Marks, I. Banakh, P. Jagadeesan, N. R. Cameron, C. Yung-Chih, M. Costa, K. Peter, H. Cleland, S. Akbarzadeh, A platelet-derived hydrogel improves neovascularisation in full thickness wounds, Acta Biomater. 136 (2021) 199–209, https://doi.org/10.1016/j.actbio.2021.09.043.
[68] B.Z. Johnson, A.W. Stevenson, C.M. Prêle, M.W. Fear, F.M. Wood, The role of IL-6 in skin fibrosis and cutaneous wound healing, Biomedicines 8 (5) (2020) 101, https://doi.org/10.3390/biomedicines8050101.